Triaxial nuclear shapes in ^{126}I

Bhushan Kanagalekar, Pragya Das,* and Bhushan Bhujang
Department of Physics, Indian Institute of Technology Bombay, Powai, Mumbai 400076, India

S. Muralithar, R. P. Singh, and R. K. Bhowmik
Inter-University Accelerator Centre, Aruna Asaf Ali Marg, New Delhi 110067, India

(Received 19 July 2012; revised manuscript received 22 December 2012; published 7 November 2013)

The energy levels of the odd-odd nucleus ^{126}I have been investigated by in-beam γ-ray spectroscopic techniques. Twenty seven new γ transitions have been identified. The polarization analysis was carried out using the clover detector as a Compton polarimeter. We have made definite parity assignments to six bands. Five of them were in agreement with the previous assignments of parity, but one band for which the theoretical interpretation was earlier reported with an assumed negative parity [Zheng *et al.*, Phys. Rev. C **86**, 014320 (2012)] was found to be of positive parity. We have carried out the theoretical analysis of different bands using the particle rotor model and the calculations of the total Routhian surface. The signature inversion observed in the yrast negative-parity band has been understood as the change in the axis of rotation from the shortest to the intermediate axis of the triaxial nucleus. Two positive-parity bands based on the particle configuration $\pi h_{11/2} \otimes \nu h_{11/2}$, have been found to be good candidates for the chiral partner behavior.

DOI: 10.1103/PhysRevC.88.054306 PACS number(s): 23.20.Lv, 21.60.−n, 21.10.−k, 25.70.−z

I. INTRODUCTION

Many nuclei in the mass region $A \sim 130$ have been studied extensively for their nuclear structure properties, because of the importance of the intruder orbit $h_{11/2}$ for the valence proton and neutron. These studies have revealed interesting phenomena such as signature splitting, signature inversion, chiral behavior, and decoupled bands. The examples are $_{55}$Cs [1], $_{57}$La [2,3], $_{59}$Pr [4,5], and $_{61}$Pm [6] nuclei. In these nuclei, the proton Fermi surface lies in the lower part of the $h_{11/2}$ subshell, while the neutron Fermi surface lies in the middle or upper part of the $h_{11/2}$ subshell. The yrast and yrare states are built on the particle configuration $\pi h_{11/2} \otimes \nu h_{11/2}$. However, for the doubly odd nucleus, $_{53}$I, the proton Fermi level may lie below the $h_{11/2}$ subshell which raises the relative energy of the $\pi h_{11/2} \otimes \nu h_{11/2}$ configuration and allows the competition from the other two quasiparticle configurations. Furthermore, when the valence neutron starts to occupy the high-Ω orbitals of the $h_{11/2}$ subshell, the deformation-driving properties of protons and neutrons become different. As a result, a given nucleus may have either a prolate, an oblate, or a triaxial shape, depending on the configuration. In this respect, the odd-odd nucleus ^{126}I is of interest.

Early investigations on ^{126}I were limited to low spin states via the reactions ^{126}Te$(p, n)^{126}$I [7], ^{127}I$(n, 2n)^{126}$I [8], and ^{127}I$(\gamma, n)^{126}$I [9]. There was an unpublished result [10] based on an experiment performed using the heavy-ion fusion reaction ^{124}Sn(^{7}Li, $5n)^{126}$I. Although well-developed band structures were reported, the theoretical results were tentative. Later, an excited positive-parity band was theoretically analyzed and assigned the particle configuration $\pi h_{11/2} \otimes \nu h_{11/2}$ by Moon [11]. A partial level scheme was published by Li *et al.* [12]. A recent publication by Zheng *et al.* [13] has confirmed the seven bands presented in Ref. [10] with the addition of some new transitions. They have assigned the particle configurations to various bands with the help of the triaxial projected shell model and the cranked shell-model calculations. In the absence of any experimental evidence, their parity assignments to the states were tentative.

The work presented here describes the experimental findings of the energy levels of ^{126}I. We have used the same heavy-ion reaction as in the earlier works [10,13]. Triple- and double-γ coincidences were recorded using 15 high-purity germanium (HPGe) clover detectors. The advantage of using the clover detector was the utilization of its four segments as a Compton polarimeter for the polarization analysis. The positive (negative) value of the polarization asymmetry parameter corresponds to the electric (magnetic) nature of the γ rays. Thus, the parity of the states was experimentally determined for the first time. One of the bands, assumed to be of negative parity by Zheng *et al.* [13] in their theoretical treatment, was found to have a positive parity in our experimental investigation. In the entire decay scheme, our placement of γ transitions and the spins of the levels agreed to a large extent with the earlier works [10,13]. However, some of the placements have been changed because of newly found interlinking transitions.

Understanding the nuclear behavior, influenced by changing deformation with increasing angular momentum, can be quite a challenge. The phenomenological particle rotor model (PRM), which is based on the concept of valence particles coupled to a rotating core, has been widely used in the mass region 130 in the past [14]. The success of any such model-dependent theoretical calculation largely depends on the input parameters. The crucial parameters are the quadrupole deformation (ε_2) and the triaxiality parameter (γ) of the rotating core nucleus. The total energy minimum in the contour plot of the total Routhian surface (TRS) calculation gives a reliable estimate of the deformation parameters (ε_2, γ) of the core nucleus. The quasiparticle energy diagrams provide an initial

*pragya@phy.iitb.ac.in

guess for the lowest occupied Nilsson orbits for the valence particles, which are yet another important input to the PRM. We have carried out the theoretical investigation of different bands in the framework of TRS and PRM calculations.

The observed phenomenon of signature inversion in the yrast band has been understood as the change in the axis of rotation from the shortest to the intermediate axis of the triaxial core nucleus, by following the arguments of Ikeda and Åberg [15]. Interestingly, the same cause for the signature inversion has been discussed for $_{55}$Cs nuclei by Gao *et al.* [16] by using the triaxial projected shell model. Our assignment of the valence particle configuration $\pi d_{5/2} \otimes \nu h_{11/2}$ to this band agreed with that of Zheng *et al.* [13], but was in contradiction to that of Moon *et al.* [10].

We have proposed two excited positive-parity bands, based on the particle configuration $\pi h_{11/2} \otimes \nu h_{11/2}$, for the candidature of chirality. Zheng *et al.* [13] assumed one of these excited bands to have negative parity. They then theoretically interpreted the same excited band to be the chiral partner of the yrast negative-parity band above $15\hbar$. Therefore, our result on chirality for ^{126}I is in marked contrast with theirs.

II. EXPERIMENT AND RESULTS

In the present experiment, high spin states of ^{126}I were populated using the reaction ^{124}Sn(^{7}Li, $5n$)^{126}I at the beam energy of 50 MeV. The measurement was carried out at the 15UD Pelletron accelerator at the Inter-University Accelerator Centre (IUAC), New Delhi, India. An isotopically enriched (99.9%) self-supporting ^{124}Sn target of thickness 2.7 mg/cm^2 was used so that most of the recoiling evaporation residues stopped in the target itself. The γ rays emitted in the reaction were detected by the Indian National Gamma Array (INGA) [17], consisting of 15 Compton suppressed HPGe clover detectors arranged in five rings. Three detectors were placed at 32°, two at 57°, four at 90°, two at 123°, and four at 148° with respect to the beam direction. The triple-γ coincidence data were collected in the event-by-event mode, called the list mode. For this purpose, a CAMAC-based multichannel synchronization mode was utilized with an in-house software CANDLE [18] on the Linux platform.

The data were initially sorted using the computer program LAMPS [19]. The energy calibration (0.5 keV per channel) of the list mode data was done using a radioactive source ^{152}Eu. The background subtracted data were then utilized to generate different types of $4k \times 4k$ matrices. Each of these matrices were used to extract different experimental results. For example, one matrix was E_γ vs E_γ, in which each of the two axes corresponded to the energy of the coincident γ rays measured by any two clover detectors in the add-back mode [20]. In this mode, much of the Compton background was reduced by appropriately adding the events corresponding to the Compton scattering to the events corresponding to the photopeak. The symmetrized matrix was generated by making the two energy axes equivalent. From this matrix, the projected spectra with the individual γ-energy gate were generated. The projected spectrum with the full-energy gate, called the total projected spectrum, was also generated for the visual examination of the γ-ray intensities. Of all the residues, ^{126}I was most dominantly

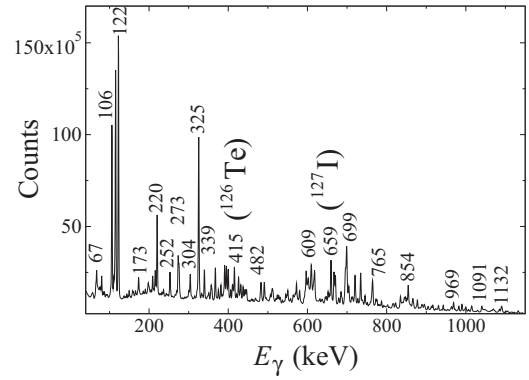

FIG. 1. Total projected γ-ray spectrum. The labeled γ transitions belong to ^{126}I. The γ peaks of 415 and 659 keV belonging to other intensely populated residues are also marked.

populated. This is evident from the total projected spectrum shown in Fig. 1, in which most of the intense, labeled γ transitions belong to ^{126}I. To obtain the directional correlation ratio (DCO), an asymmetric E_γ vs E_γ matrix was constructed from the coincidence data with γ-ray energies from detectors at 32° and 148° on one axis and those from 90° on the other axis. Two asymmetric matrices for parallel and perpendicular scattering of the γ ray were prepared for the polarization analysis. In such a matrix, one axis corresponded to scattered γ ray and other axis to the coincident γ ray detected by the remaining clovers in the add-back mode. The data were analyzed using the computer program RADWARE [21,22].

We discuss below the construction of the level scheme, the determination of the spins of the energy states by the analysis of the DCO, and the assignment of the parity by polarization measurements. The experimental results are summarized in Table I.

A. Level scheme

The level scheme of ^{126}I (Fig. 2), deduced in the present work, was based on the γ-ray coincidence and intensity relationships. To illustrate the placement of new γ transitions in the decay scheme, we present here examples of the projected spectra, shown in Figs. 3 and 4. In these spectra, the new γ peaks (shown in red) and some intense γ transitions belonging to ^{126}I have been labeled. However, some close-by intense peaks have not been labeled to maintain the clarity of these figures. Also, there are unlabeled peaks belonging to ^{126}I which were known earlier [10,13] and have not been further studied by us. A few small contaminant peaks belonging to the neighboring nuclei are also present in the spectra. These projected spectra were generated by putting the double-γ gates on the triple-γ coincidence data. To enhance the intensity of the peaks in the projected spectra, we have added a few projected spectra. Our notation for the double-γ gate is $\gamma 1/\gamma 2$, where $\gamma 1$ and $\gamma 2$ denote the energy, in keV, of the gates corresponding to the two γ transitions.

Figure 3(a) shows the sum of the projected spectra of 375/410, 469/252, and 252/727. This spectrum shows the presence of the two coincident γ transitions of energies 258 and 1081 keV. These two new γ transitions have been placed in Band 5.

TABLE I. Energy, intensity (normalized to intensity of the 122.2-keV transition), gate for the DCO, DCO ratio, experimental asymmetry (Δ), mixing ratio, multipolarity, initial and final state spin of the transitions of ^{126}I, deduced from the present work, are listed. The error in E_γ is $\pm$0.5 keV. The errors for the other quantities are statistical and mentioned in brackets.

Energy (E_γ)	Intensity (I_γ)	Gating transition (keV)	DCO ratio	Asymmetry (Δ)	Mixing ratio (δ)	Multipolarity	Assigned $J_i^\pi \rightarrow J_f^\pi$
51.8							$12^+ \rightarrow 11^+$
66.6	39(14)	122	0.57(3)		0.16(3)	$M1/E2$	$7^- \rightarrow 6^-$
79.9	17(5)	699	0.82(4)		0.25(3)	$M1/E2$	$10^+ \rightarrow 9^+$
105.6	80(19)	122	0.65(1)		0.25(1)	$M1/E2$	$8^- \rightarrow 7^-$
115.1	94	734	1.27(2)		0.23(1)	$E2/M3$	$6^- \rightarrow 4^-$
122.2	100	734	1.31(2)		0.24(3)	$E2/M3$	$4^- \rightarrow 2^-$
135.8							$9^- \rightarrow 8^-$
137.0							$21^- \rightarrow 20^-$
149.5	5(1)						$22^+ \rightarrow 21^+$
151.8	0.8(2)						$13^- \rightarrow 12^-$
157.8	2.8(6)						$9^- \rightarrow 8^-$
165.2	2.4(5)						$11^- \rightarrow 10^-$
173.3	12(3)	720	0.92(6)			$E2$	$8^- \rightarrow 6^-$
176.7							$17^+ \rightarrow 16^+$
184.7	1.8(4)						$17^- \rightarrow 16^-$
208.1	1.3(3)						$18^+ \rightarrow 17^+$
211.6	2.4(5)						$13^{(+)} \rightarrow 12^+$
216.7	2.6(6)						$17^- \rightarrow 16^-$
219.7		877	0.70(4)		0.14(3)	$M1/E2$	$12^+ \rightarrow 11^+$
220.0	33(7)	666	1.22(6)		0.23(3)	$M1/E2$	$15^+ \rightarrow 14^+$
252.3	10(2)	877	0.68(7)		0.10(6)	$M1/E2$	$14^+ \rightarrow 13^+$
258.4	0.6(2)						$16^{(+)} \rightarrow 15^{(+)}$
273.0	22(5)	122	0.49(1)	$-0.01(1)$	0.09(2)	$M1/E2$	$8^- \rightarrow 7^-$
275.4	10(2)	787	0.70(6)		0.14(5)	$M1/E2$	$13^+ \rightarrow 12^+$
299.6	3.6(8)						$12^+ \rightarrow 11^+$
300.5							$23^- \rightarrow 22^-$
303.6	11(2)	367	0.99(2)		0.02(2)	$M1/E2$	$14^+ \rightarrow 13^+$
324.9	90(20)	734	0.47(1)	$-0.04(1)$	$-0.06(1)$	$M1/E2$	$9^- \rightarrow 8^-$
327.8	2.8(6)						$16^{(+)} \rightarrow 15^+$
339.2	16(4)	720	0.48(1)	$-0.06(1)$	$-0.05(2)$	$M1/E2$	$11^- \rightarrow 10^-$
350.6	1.0(3)	894	0.59(4)		0.04(4)	$M1/E2$	$18^- \rightarrow 17^-$
356.2	7(2)	772	1.48(6)	0.05(2)	0.13(3)	$E1/M2$	$10^+ \rightarrow 9^-$
366.9	18(4)	523	1.74(8)	$-0.03(1)$	0.02(3)	$M1/E2$	$13^+ \rightarrow 12^+$
374.5	5(1)	765	0.38(2)		$-0.18(3)$	$M1/E2$	$14^{(+)} \rightarrow 13^{(+)}$
381.9							$11^+ \rightarrow 11^+$
384.8	2.7(6)	854	0.48(4)		$-0.07(4)$	$M1/E2$	$16^- \rightarrow 15^-$
387.0	3.1(7)						$20^- \rightarrow 19^-$
387.1		275	0.82(6)		0.00(4)	$M1/E2$	$16^+ \rightarrow 15^+$
390.5	17(4)	523	1.71(11)	$-0.05(1)$	0.04(3)	$M1/E2$	$16^+ \rightarrow 15^+$
394.9	21(4)	325	0.50(1)	$-0.03(2)$	$-0.05(1)$	$M1/E2$	$10^- \rightarrow 9^-$
399.6	19(4)	670	1.20(8)		0.25(3)	$M1/E2$	$11^+ \rightarrow 10^+$
399.6		1085	0.78(6)		$-0.07(5)$	$M1/E2$	$15^+ \rightarrow 14^+$
410.2	3.6(8)	751	0.54(2)		$-0.19(2)$	$M1/E2$	$15^{(+)} \rightarrow 14^{(+)}$
410.8							$9^+ \rightarrow 8^{(-)}$
415.1	2.3(5)						$18^+ \rightarrow 17^+$
420.2	2.4(5)	751	0.57(3)		$-0.16(3)$	$M1/E2$	$16^{(+)} \rightarrow 15^{(+)}$
425.6	15(3)	734	0.45(2)	$-0.09(1)$	$-0.09(2)$	$M1/E2$	$12^- \rightarrow 11^-$
429.1							$13^- \rightarrow 12^-$
430.9	1.6(3)						$9^- \rightarrow 7^-$
437.1	9(2)	854	0.37(1)	$-0.07(1)$	$-0.19(2)$	$M1/E2$	$14^- \rightarrow 13^-$
442.7	3.9(8)	1091	0.73(6)		0.14(4)	$M1/E2$	$20^+ \rightarrow 19^+$
468.6							$15^{(+)} \rightarrow 14^+$
481.2							$19^+ \rightarrow 18^+$
482.9							$18^+ \rightarrow 17^+$

TABLE I. (*Continued.*)

Energy (E_γ)	Intensity (I_γ)	Gating transition (keV)	DCO ratio	Asymmetry (Δ)	Mixing ratio (δ)	Multipolarity	Assigned $J_i^\pi \rightarrow J_f^\pi$
490.1	2.7(6)	252	0.72(3)		−0.12(3)	$M1/E2$	$17^+ \rightarrow 16^+$
494.7	2.8(6)	252	1.72(10)			$E2$	$13^+ \rightarrow 11^+$
509.6							$17^- \rightarrow 16^-$
523.3	5(1)					$E2$	$15^+ \rightarrow 13^+$
526.6	5(1)						$16^- \rightarrow 15^-$
527.6		220	1.31(9)			$E2$	$14^+ \rightarrow 12^+$
530.5	4(1)						$21^+ \rightarrow 20^+$
531.1							$8^- \rightarrow 8^-$
531.4							$15^- \rightarrow 14^-$
550.6	1.6(3)						$15^- \rightarrow 14^-$
554.3	1.1(2)						$16^- \rightarrow 15^-$
566.4							$19^+ \rightarrow 18^+$
568.7	7(2)						$10^- \rightarrow 9^-$
571.9	11(2)	1006	1.11(7)	0.12(8)		$E2$	$19^- \rightarrow 17^-$
577.9							$13^+ \rightarrow 12^+$
578.9	2.8(6)	711	0.52(6)		−0.04(5)	$M1/E2$	$15^- \rightarrow 14^-$
601.6	12(3)	275	0.88(5)	−0.02(2)	0.20(4)	$M1/E2$	$12^+ \rightarrow 11^+$
608.9		391	0.89(3)		0.09(2)	$M1/E2$	$17^+ \rightarrow 16^+$
609.8							$19^- \rightarrow 18^-$
609.8							$16^+ \rightarrow 14^+$
617.6	28(6)	325	0.50(1)	−0.07(1)	−0.21(3)		$9^+ \rightarrow 9^-$
637.0	0.8(2)						$8^- \rightarrow 7^-$
644.4	7(2)	122	1.94(4)		0.10(2)	$M1/E2$	$10^- \rightarrow 9^-$
647.3	6(1)						$11^+ \rightarrow 10^+$
651.5	2.0(4)	275	1.51(9)			$E2$	$15^+ \rightarrow 13^+$
666.2	9(2)	122	0.69(3)	0.13(5)		$E2$	$13^+ \rightarrow 11^+$
666.4							$9^- \rightarrow 8^-$
668.7							$12^- \rightarrow 11^-$
670.3	28(6)	699	0.87(2)	0.09(2)		$E2$	$14^+ \rightarrow 12^+$
679.5	2.0(4)						$22^+ \rightarrow 20^+$
684.1	3.3(7)	572	0.49(2)		−0.07(3)	$M1/E2$	$20^- \rightarrow 19^-$
698.1							$10^+ \rightarrow 9^-$
699.0	50(11)	618	0.87(3)			$E2$	$12^+ \rightarrow 10^+$
704.1	10(2)	765	1.55(9)		0.09(3)	$M1/E2$	$13^- \rightarrow 12^-$
711.1	7(2)	572	1.03(6)	0.17(3)		$E2$	$17^- \rightarrow 15^-$
719.6	29(6)	765	0.89(3)	0.11(1)		$E2$	$10^- \rightarrow 8^-$
726.6	9(2)	273	1.59(8)			$E2$	$10^- \rightarrow 8^-$
726.8							$(16^{(+)}) \rightarrow 14^+$
733.9	36(8)	854	0.92(3)	0.13(1)		$E2$	$11^- \rightarrow 9^-$
739.0	3.0(7)	572	0.93(7)			$E2$	$17^- \rightarrow 15^-$
750.9	5(1)	765	0.78(6)		0.19(4)	$E1/M2$	$13^{(+)} \rightarrow 12^-$
758.2	4.0(9)	325	0.53(1)			$E2$	$12^- \rightarrow 10^-$
764.5	17(4)	720	0.88(3)	0.06(1)		$E2$	$12^- \rightarrow 10^-$
772.2	9(2)	122	0.66(3)	−0.03(6)		$E2$	$9^- \rightarrow 7^-$
775.7	6(1)	115	0.41(5)	0.17(6)	−0.03(6)	$E1/M2$	$9^+ \rightarrow 8^-$
781.5	3.1(7)						$11^+ \rightarrow 10^+$
786.6	3.7(8)	252	1.55(10)			$E2$	$16^+ \rightarrow 14^+$
799.5	0.9(2)						$22^- \rightarrow 21^-$
802.0							$10^- \rightarrow 8^-$
815.0	2.6(6)	252	0.70(7)	0.06(2)	−0.12(6)	$E1/M2$	$13^+ \rightarrow 12^-$
816.7							$15^- \rightarrow 14^-$
821.5	3.5(7)	572	0.95(5)	0.14(12)		$E2$	$21^- \rightarrow 19^-$
822.6							$16^+ \rightarrow 15^+$
830.1							$16^{(+)} \rightarrow 14^{(+)}$
834.6	10(2)	220	0.89(6)		0.09(4)	$E1/M2$	$11^+ \rightarrow 10^-$
844.6	9(2)	854	0.56(5)		0.00(4)	$M1/E2$	$15^- \rightarrow 14^-$

TABLE I. (*Continued*.)

Energy (E_γ)	Intensity (I_γ)	Gating transition (keV)	DCO ratio	Asymmetry (Δ)	Mixing ratio (δ)	Multipolarity	Assigned $J_i^\pi \rightarrow J_f^\pi$
854.1	27(6)	734	0.90(3)	0.11(2)		$E2$	$13^- \rightarrow 11^-$
860.0	3.7(8)						$18^- \rightarrow 16^-$
865.8	12(3)						$14^- \rightarrow 12^-$
867.5	5(1)	273	1.48(17)			$E2$	$12^- \rightarrow 10^-$
877.2	1.9(4)	275	0.71(7)			$E2$	$17^+ \rightarrow 15^+$
883.8	2.1(5)						$17^+ \rightarrow 16^+$
888.7	6(1)	325	0.54(1)			$E2$	$14^- \rightarrow 12^-$
894.2	4.1(9)	854	0.95(11)			$E2$	$17^- \rightarrow 15^-$
904.9	2.5(5)	787	0.96(9)			$E2$	$18^+ \rightarrow 16^+$
910.6	1.0(2)	220	0.86(15)		0.07(8)	$E1/M2$	$11^+ \rightarrow 10^-$
916.0	4.6(9)	854	0.79(8)			$E2$	$16^- \rightarrow 14^-$
923.7	1.4(3)						$20^+ \rightarrow 18^+$
942.4	8(2)	122	1.69(5)	0.04(1)	0.19(2)	$E1/M2$	$9^+ \rightarrow 8^-$
960.0	1.9(4)						$19^- \rightarrow 17^-$
960.0							$20^+ \rightarrow 18^+$
963.5	5(1)	999	0.89(9)			$E2$	$19^+ \rightarrow 17^+$
968.5	11(2)	854	0.92(4)			$E2$	$15^- \rightarrow 13^-$
973.1	2.7(6)	391	1.67(24)			$E2$	$21^+ \rightarrow 19^+$
978.4	1.2(3)						$15^- \rightarrow 13^-$
981.6							$19^+ \rightarrow 17^+$
995.6	1.9(4)						$20^- \rightarrow 18^-$
999.2	7(1)	670	0.83(6)			$E2$	$17^+ \rightarrow 15^+$
1000.2							$14^- \rightarrow 12^-$
1006.3	3.4(7)						$15^- \rightarrow 13^-$
1007.7							$12^- \rightarrow 10^-$
1042.5							$16^+ \rightarrow 14^+$
1072.5	2.6(6)						$16^- \rightarrow 14^-$
1081.2	1.2(3)						$(17^{(+)}) \rightarrow (16^{(+)})$
1084.5	5(1)	720	1.59(10)	0.07(3)	0.09(3)	$E1/M2$	$11^+ \rightarrow 10^-$
1091.4	5(1)						$18^+ \rightarrow 16^+$
1100.2	2.5(5)						$23^- \rightarrow 21^-$
1104.8	2.5(5)						$16^- \rightarrow 14^-$
1131.9	3.0(6)						$14^- \rightarrow 12^-$
1253.7							$15^- \rightarrow 13^-$

Figure 3(b) shows the sum of the projected spectra of 758/273 and 889/273. The new transition of energy 802 keV interlinking Band 1 and Band 2 was identified.

The identification and placement of the weak γ transitions 566, 578, 960, and 982 keV belonging to Band 6 were done by creating many combinations of sum spectra. One example of such spectra is shown in Fig. 3(c). The gates were 400/387, 252/905, and 252/387.

Figure 3(d)–3(f) are the examples of the γ transitions belonging to Band 7. In Fig. 3(d), the gates were 220/884, 220/391, and 391/884. This spectrum identified the presence of new transitions 884 and 208 keV, placed above 16^+. However, the placement of the 208-keV transition was tentative because of its weak intensity. Similarly, the weak 177-keV transition was identified by gating on 220/823, as shown in Fig. 3(e). Another projected spectrum, with the sum of double gates 220/367, 220/699, 304/699, and 304/367, was created to identify the new γ transitions of energies 177, 823, 884, and 1043 keV [Fig. 3(f)].

There were inconsistencies in the placement of some γ transitions in Band 4 in the earlier two references [10,13]. Our data analysis agreed with the placement of the 572-keV γ transition done by Zheng *et al*. [13]. However, their claim of the 684-keV transition being in coincidence with the 822-keV transition did not agree with our data. We found these two transitions to decay to the same level 19^-, as was proposed by Moon *et al*. [10]. A set of projected spectra was generated by taking two simultaneous gates on the γ transitions. The examples of the sum of the projected spectra are shown in Fig. 4. Figure 4(a) shows the sum spectrum of 572/185, 185/1132, 572/889, and 185/889. Similarly Fig. 4(b) is for 572/889 and 572/1073, and Fig. 4(c) is for 734/854 and 739/854. The new γ transitions 217, 551, 554, 579, 1105, and 1254 keV and a new spin-state 16^- in Band 4 were identified.

The relative intensities of the γ transitions were determined using the most intense γ peak of energy 122 keV as the reference, by assuming its intensity to be 100. Two independent gates of energies 115 and 122 keV were put in the double

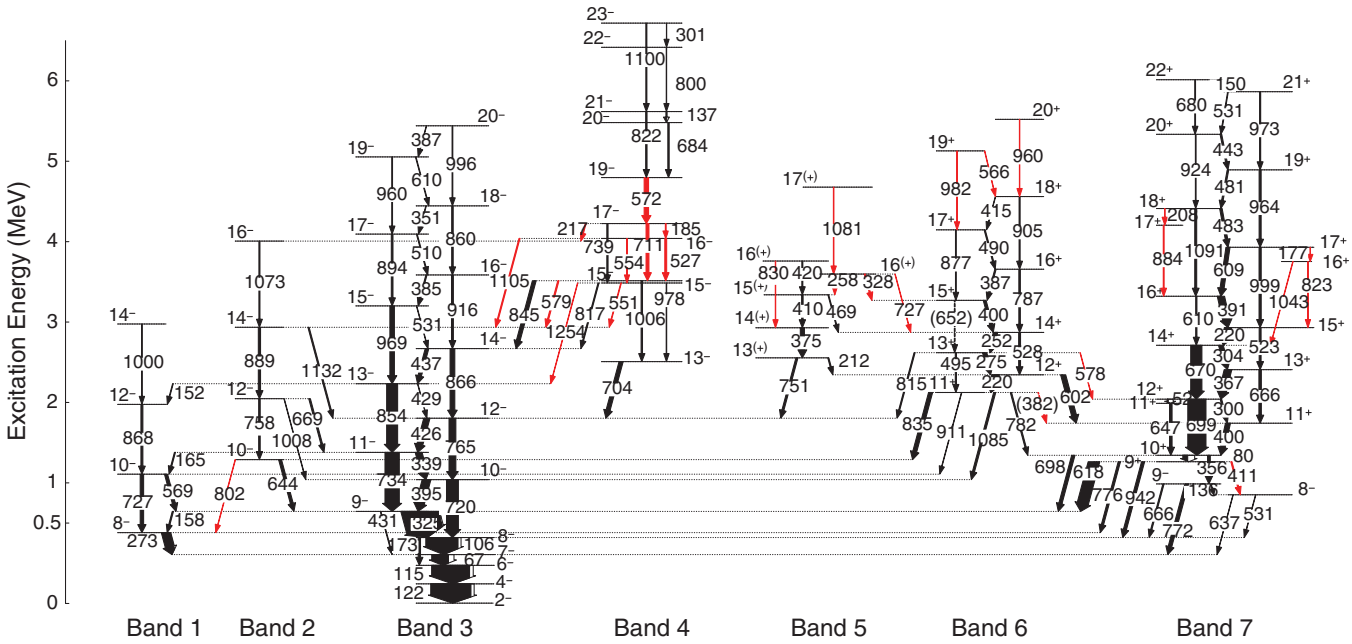

FIG. 2. (Color online) Level scheme of ^{126}I. The energies of the transitions are shown in keV. The new γ transitions are marked in red.

coincidence data. From the two projected spectra, the ratio of the efficiency-corrected intensities for a particular γ transition was found to have a nearly constant value of 0.94 for many intense transitions. Thus the intensity of the 115-keV transition was determined to be 94. The same procedure was applied for finding the intensities of the other γ transitions with lower-lying transitions as gates. Table I shows the results.

B. Spin

The multipolarity and the mixing ratio of the γ transitions were deduced from the DCO ratio. In the most effective approach for finding the DCO ratios, one of the coincident detectors should be close to $\theta = 0^\circ$ or 180° and the other close to $\theta = 90^\circ$. For the same reason, ϕ should be close to 0° or 180° [23]. Accordingly, we constructed an asymmetric matrix with one axis corresponding to the detectors at $\theta = 90^\circ$ and the other axis corresponding to the detectors at $\theta = 32^\circ$ and 148° and $\phi = 0^\circ$ and 180°. Here, θ is the angle subtended by the detector with the beam direction and ϕ is the angle between the two planes opened by each detector and the beam axis. The experimental DCO ratios were calculated using Eq. (1) [24]:

$$R_{\mathrm{DCO}} \equiv \frac{I^{\gamma_2}_{\theta_1}(\mathrm{gate}^{\gamma_1}_{\theta_2})}{I^{\gamma_2}_{\theta_2}(\mathrm{gate}^{\gamma_1}_{\theta_1})}, \qquad (1)$$

where $I^{\gamma_2}_{\theta_i}(\mathrm{gate}^{\gamma_1}_{\theta_j})$ is the intensity of γ_2 detected at θ_i, in coincidence with γ_1 detected at θ_j, for $i, j = 1, 2$; $i \neq j$.

The experimentally determined values of the DCO ratios were compared with the theoretical curves to determine the multipolarity of the transition. Assuming that the nature of transitions is pure and stretched, the DCO ratios are expected to be close to 1.0 for a quadrupole transition and 0.5 for a dipole transition, when the gate is set on a quadrupole transition. In the case of gating on a dipole transition, DCO ratios of approximately 1.5 for a stretched quadrupole ($L = 2$, $\Delta I = 2$) transition and of 1.0 for a stretched dipole ($L = 1$, $\Delta I = 1$) transition are expected, where I and L are the spin of the state and the multipolarity of the transition, respectively.

The theoretical prescription of DCO ratios was given by Krane *et al.* [23]. According to this theory, the nuclei produced in the heavy-ion reaction are aligned in their angular momentum, and the alignment parameter σ measures the degree of alignment. Two coincident γ rays in a cascade, emitted by these nuclei and detected at different angles, show a definite pattern in their intensity ratios. The DCO ratio not only depends on the nature of the decaying transitions but also on the mixing ratio δ of both the transitions in the cascade. If the lowest multipolarity of a particular transition is $E2$, the mixing of $M3$ is normally very small and $\delta = 0$ may be assumed. In our calculations, the value of the alignment parameter σ/I was assumed to be 0.3. The theoretical DCO curves were plotted as a function of $\tan^{-1}\delta$ for different values of the unknown spin I. By comparing the experimental values of R_{DCO} with the theoretical DCO plots, the unknown spin I was determined. For the ambiguous cases, when the theoretical curve matched with the experimental value of R_{DCO} at two different values of δ, another decay path involving the same unknown spin state was analyzed. A consistent matching, through both the decay paths, was invariably found for the lower value of δ. In any case, the value of unknown spin I was finally decided such that its value did not decrease with increasing excitation energy.

Figures 5(a), 5(b), and 5(c) were the typical examples involving the 1085- and 776-keV transitions which interlinked two different bands. Such transitions played an important role in establishing the spins of the entire Band 6 and Band 7, in agreement with the earlier [10,13] tentative assignment. Moreover, these figures are the representatives of a three-level decay and a four-level decay, each with one unknown value of spin I. The hatched region represents the experimental value of the DCO with its error. The error was estimated from the

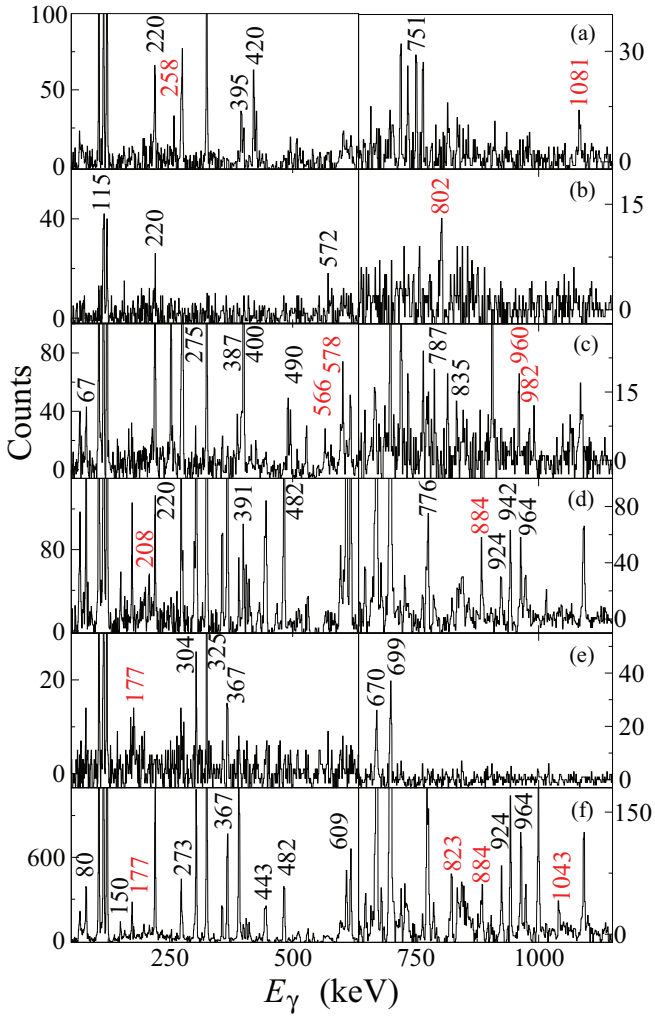

FIG. 3. (Color online) Examples of the projected spectra obtained using double-γ gates on the triple-γ coincidence data. The labeled γ-transitions belong to ^{126}I. Peaks marked in red are new transitions observed in the present study. The detailed description is given in the text.

uncertainty obtained in the areas of the γ peaks. In Fig. 5(a), the curves corresponding to $I = 11$ and $I = 10$ matched the experimental $R_{\rm DCO}$ at the low and the high δ values, respectively. On the other hand, when a different sequence of γ transitions was utilized, as shown in Fig. 5(b), $I = 11$ was the only choice. The state decaying via the 776-keV transition was found to be $I = 9$, as shown in Fig. 5(c). Thus the multipolarities of both the 1085- and 776-keV transitions were confirmed to be dipole. Similar analysis was done for the other intense cascades of γ transitions and the results are summarized in Table I.

C. Parity

The parity of the energy states was determined by the polarization measurement. The polarization of a γ transition, defined as $P \equiv \Delta/Q$, is related to the experimental asymmetry Δ and the polarization sensitivity Q of the polarimeter. The functional dependence of Q on the energy of the photon, E_γ,

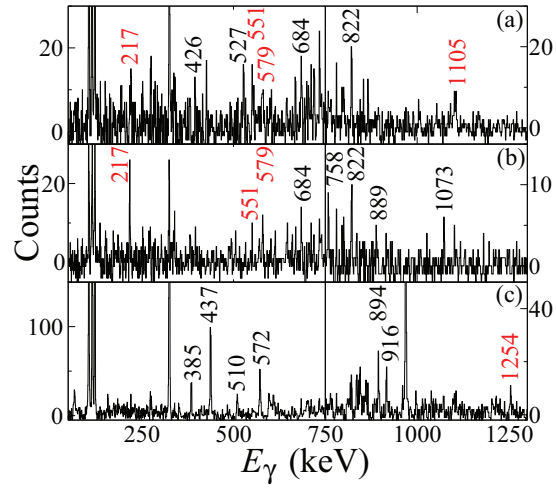

FIG. 4. (Color online) The projected spectra obtained by the double-γ gates on the triple-γ coincidence data. The labeled γ-transitions belong to ^{126}I. The new γ transitions, marked in red, connect Band 4 with other bands. The details have been discussed in the text.

and the finite size of the detector has been discussed by Schmid *et al.* [25]. An extensive study characterizing the various aspects of the clover detectors has been described by Duchêne *et al.* [26]. A typical measurement of Q, in the energy range of 386 to 1368 keV for the type of the clover detector used in the INGA, was performed by Palit *et al.* [27]. For a Compton polarimeter, the experimental asymmetry Δ is defined as

$$\Delta \equiv \frac{aN_\perp - N_\parallel}{aN_\perp + N_\parallel}, \tag{2}$$

where $N_\parallel$ ($N_\perp$) is the number of detected γ rays undergoing the Compton scattering parallel (perpendicular) to the reaction plane. The reaction plane is defined as the plane containing the incident beam direction and the outgoing γ ray. The parameter a is a measure of asymmetry in the response of the perpendicular and the parallel crystals and is defined as

$$a \equiv \frac{N_\parallel(\text{unpolarized})}{N_\perp(\text{unpolarized})}. \tag{3}$$

Often it is possible to distinguish between the electric and the magnetic type of transitions from the measured value of Δ. In a clover detector, one of the segments acts as a scatterer and the other segments act as an analyzer, constituting a Compton polarimeter. In our experimental setup, the detector at 90° was found to be the most suitable as a Compton polarimeter. In this detector, when one of the coincident γ rays was incident on any of its segments and underwent Compton scattering in the segment parallel (perpendicular) to the reaction plane, the event was recorded as $N_\parallel$ ($N_\perp$). The other coincident γ ray was detected in any of the other clover detectors of the array. To extract the polarization asymmetry Δ from our data, two asymmetric matrices, corresponding to the parallel and perpendicular scattering, were created. They were called parallel and perpendicular matrices. These matrices were then utilized to generate the projected spectra with gates on the strong transitions of ^{126}I. The intensity of a particular γ

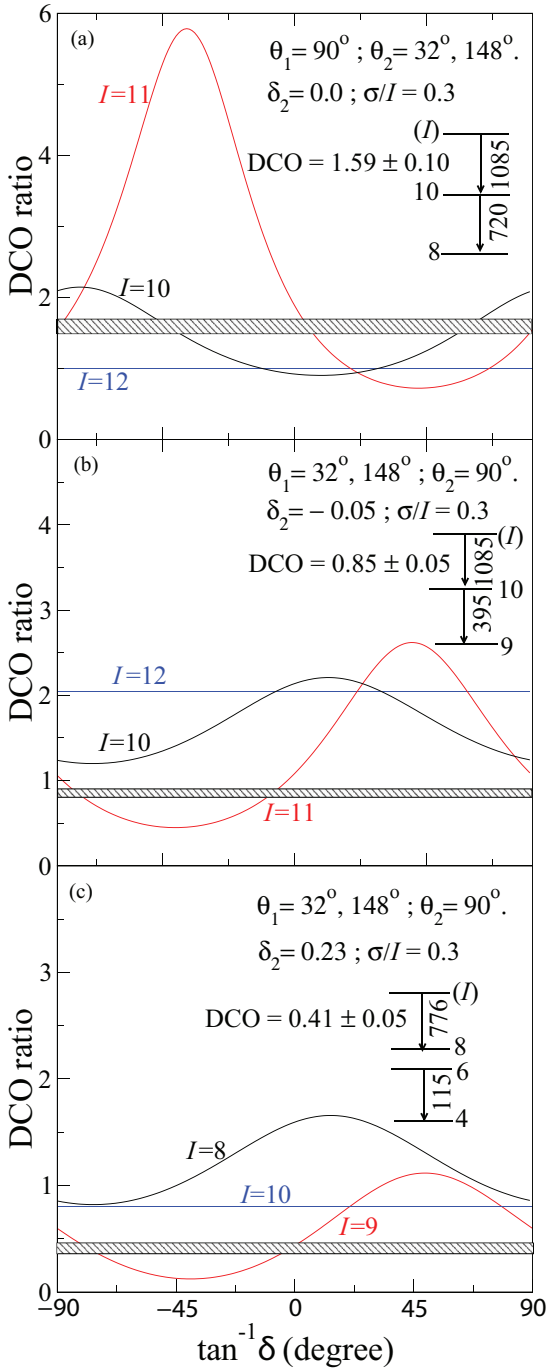

FIG. 5. (Color online) Theoretical DCO curves as a function of $\tan^{-1}\delta$ for the coincident γ transitions: (a) 1085 and 720 keV, (b) 1085 and 395 keV, and (c) 115 and 776 keV. The hatched region indicates the experimental value of the DCO.

peak obtained from the parallel and perpendicular matrices yielded $N_{\parallel}$ and $N_{\perp}$, respectively. The value of the asymmetry parameter a was obtained from the radioactive source ^{152}Eu in the energy range of 0.25 to 1.4 MeV. Roughly a constant value of $a \simeq 1$ was found. Figure 6 shows the experimental asymmetry (Δ) for many γ transitions in the level scheme. The statistical quality of the spectra was not good. Therefore, the values of Δ were obtained only for those transitions

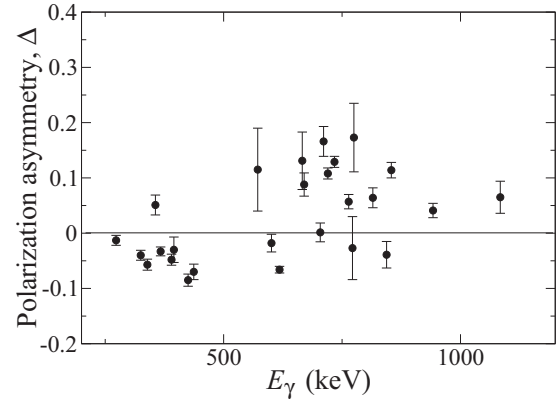

FIG. 6. Plot of experimental asymmetry (Δ) for different γ transitions measured in the present experiment.

whose gates were clean and intense. Moreover, because of the low counts corresponding to Compton scattering events at the low energy, our analysis was restricted to the minimum energy of 273 keV. The positive and negative values of Δ correspond to pure stretched electric and pure stretched magnetic transitions, respectively [28], while the opposite is true for the pure nonstretched transitions. The same sign convention is applicable for the mixed transitions, if the value of the mixing ratio is low. However, for the large mixing the sign may be opposite. Our parity assignment for most of the transitions was found to be consistent with the sign of Δ for the stretched transitions with low mixing ratio. Typical examples were the $M1/E2$ transitions, 325, 339, and 426 keV, belonging to Band 3 (see Table I). In fact, the 618-keV transition decaying from 9^+ to 9^- was the only transition found to be nonstretched. It is worth noting that we found low mixing ratios by the DCO analysis as well as by the polarization analysis for most of the observed transitions.

From the sign of Δ (Table I) and from the DCO analysis, the multipolarity of both the 1085- and 776-keV transitions was found to be predominantly of $E1$ character. Since these were the interband transitions, they played a crucial role in establishing the parity of Band 6 and Band 7. Both these bands were found to have positive parity. While our assignment of the positive parity to Band 7 agreed with that of Zheng *et al.* [13], the assignment of positive parity to Band 6 did not. Our assignment of positive parity to this band was further confirmed using the data on the 815-keV γ ray, which was another $E1$ transition connecting Band 3 to Band 6. The parity of Band 5 was tentatively assigned to be positive, because the values of Δ for the interlinking transitions could not be determined accurately.

III. THEORETICAL CALCULATIONS

We have theoretically studied the observed properties of different bands on the basis of the total Routhian surface [29,30] and the PRM calculations [31,32].

A. Total Routhian surface calculation

The general features of rotating nuclei can be understood with the Nilsson-Strutinsky prescription, in which the shell

effects and the pairing are added to the liquid-drop energy. We used the computer code ULTIMATE CRANKER [33,34] for the TRS calculation. The calculation is based on the cranking model, wherein the nucleus is assumed to be a rigid body rotating around the principal axis. For a rigid body, the moment of inertia is largest for the rotation around the shortest axis, and hence, the rotation around this axis is energetically favored. The quadrupole deformation parameter ε_2 and the triaxiality parameter γ were defined in the Lund convention [30]. In this convention, ε_2 is positive and the sign of triaxiality parameter γ defines the axis of rotation. The positive and negative values of γ correspond to the rotation around the shortest and the intermediate axis, respectively. The energy minimization was done with respect to the ε_4 parameter. The pairing gap parameters for protons and neutrons were chosen as $\Delta_p = 1.1$ MeV and $\Delta_n = 1.0$ MeV. All the other input parameters were kept at their default values.

B. Particle rotor model calculation

The PRM for the two quasiparticles, one each for the valence proton and neutron, was utilized. The computer code was procured from Ragnarsson [35]. The important inputs to the program were the single-particle orbits for the quasiparticles, the deformation parameters of the core (ε_2, ε_4, γ), and the moment of inertia parameters. The variable moment of inertia parameters were defined as A00 [$\equiv 1/(2J_0)$] and Stiff [$\equiv 1/(2J_1)$] in the Harris expansion, $\Im_0 = J_0 + J_1\omega^2$, where ω is the rotational frequency. The values of J_0 and J_1 for the neighboring even-even nucleus ^{128}Xe, taken from the table of Mariscotti *et al.* [36], were tried out first. However, the best results were obtained by the least-square fit of the Harris expansion to the yrast negative-parity band of ^{126}I itself. The values thus obtained were $J_0 = 22.4$ MeV$^{-1}\hbar^2$ and $J_1 = 36.6$ MeV$^{-3}\hbar^4$. These values were utilized for the calculations for other excited bands as well. In the hydrodynamical model, also called the irrotational flow (IRF) model, the moment of inertia $\Im_k$ is defined as

$$\Im_k \equiv \tfrac{4}{3}\Im_0 \sin^2\left(\gamma + \tfrac{2}{3}\pi k\right), \tag{4}$$

where $k = 1$, 2, and 3 correspond to the three principal axes. The IRF moment of inertia is the largest for the intermediate axis. Therefore the rotation occurs around the intermediate axis, in contrast to the rigid-body rotation around the shortest axis. To have the correct correspondence between the TRS and PRM calculations, the sign of γ was made opposite in the definition of $\Im_k$ [Eq. (4)]. This interchanged the labels of the shortest and intermediate axes. The new γ with the interchanged sign was called γ reversed. Similarly, the negative value of γ that resulted from the TRS calculation was used with the positive sign in PRM. In other words, the positive and negative values of γ (Lund convention) in the TRS calculation were used as γ reversed and positive, respectively, in the PRM. The correspondence in the sign of γ, as mentioned here, has been discussed in detail by Hamamoto and Mottelson [37] and Ikeda and Åberg [15]. Henceforth, to maintain the clarity, we discuss our results in the Lund convention only.

IV. RESULTS AND DISCUSSIONS

A. Band 3

Band 3 was found to be the most intense negative-parity band. Being the yrast band, its valence particle configuration was initially guessed by inspecting the position of the Fermi level in the Nilsson energy level diagram at moderate deformation. The valence proton was likely to occupy the positive-parity orbit below the $h_{11/2}$ subshell and the valence neutron in the negative-parity orbit $h_{11/2}$. The band exhibited the signature splitting, as shown in Fig. 11, in which the $\Delta E(\equiv [E(I) - E(I-1)] - [E(I+1) - E(I) + E(I-1) - E(I-2)]/2)$ is plotted as a function of I. The signature inversion was observed at the spin $13\hbar$. Above the inversion point, the values of ΔE for the even spins were found to be lower than those for the odd spins.

From the theoretical viewpoint, both the cranked shell model [38,39] and TRS [40,41] calculations have suggested the γ-soft core with respect to the triaxiality parameter γ for nuclei in the mass region ~130. We performed the TRS calculation for the valence proton in the positive-parity Nilsson orbit and the valence neutron in the negative-parity orbit. The contour plots were generated for all the spin values to find the deformation parameters (ε_2, ε_4, and γ) corresponding to the energy minimum. The roughly constant values of $\varepsilon_2 \sim 0.15$ and $|\gamma| \sim 45^\circ$ were found in the entire range of spins. However, the sign of γ was found to be positive at low spins and negative at high spins. In the intermediate spin range, there was fluctuation in the value and the sign of γ. Figures 7 and 8 show typical contour plots for the negative-parity yrast states at the low rotational frequency (low spin) and at the high

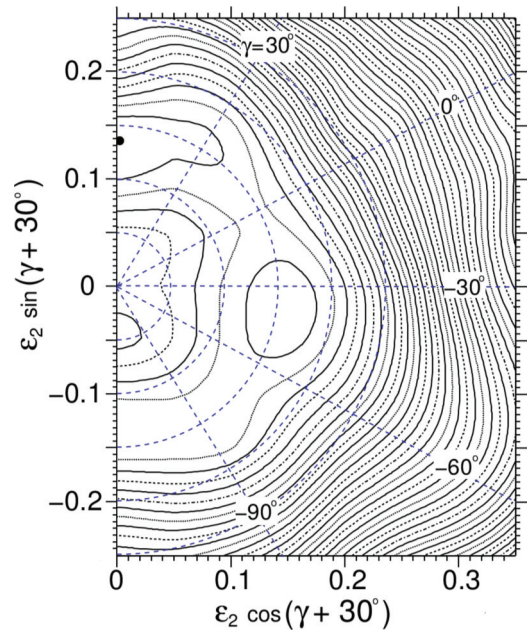

FIG. 7. (Color online) Contour plot of TRS calculations for the yrast band at the rotational frequency $\hbar\omega = 0.16$ MeV. The energy difference between the two adjacent contours is 0.2 MeV. The black dot, corresponding to the minimum energy, is at $\varepsilon_2 \simeq 0.15$, $\varepsilon_4 \simeq 0.016$, and $\gamma \simeq +55^\circ$.

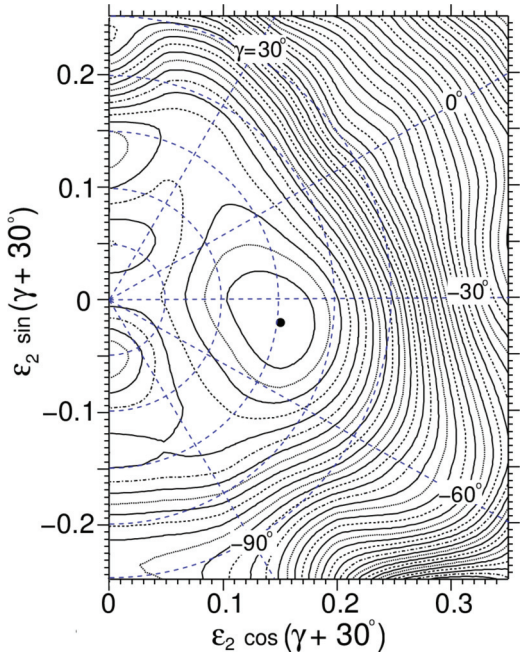

FIG. 8. (Color online) Contour plot of the TRS calculation for the yrast band at the rotational frequency $\hbar\omega = 0.33$ MeV. The energy difference between the two adjacent contours is 0.2 MeV. The black dot, corresponding to the minimum energy, is at $\varepsilon_2 \simeq 0.15$, $\varepsilon_4 \simeq 0.016$, and $\gamma \simeq -38^\circ$.

rotational frequency (high spin), respectively. The minimum energy (represented by a dot) corresponds to the deformation parameter values $\varepsilon_2 \sim 0.15$, $\varepsilon_4 \sim 0.016$, and $\gamma \sim +55^\circ$ in Fig. 7 and $\varepsilon_2 \sim 0.15$, $\varepsilon_4 \sim 0.016$, and $\gamma \sim -38^\circ$ in Fig. 8. There is a difference of 0.2 MeV between the minimum energy (shown as a dot) and the next enclosed contour. The energy difference between the two adjacent contours is also 0.2 MeV. The quasiparticle Routhian diagrams (Figs. 9 and 10) were generated at the deformation parameter values $\varepsilon_2 \simeq 0.15$, $\varepsilon_4 \simeq 0.016$, and $\gamma \simeq 55^\circ$. From the position of different orbits at the low rotational frequency, the valence particle configuration at the bandhead could be guessed. The lowest negative-parity quasineutron orbit was found to be $h_{11/2}$. For the quasiproton (Fig. 9), the lowest orbit (dotted line) was found to have a major component of $g_{7/2}$ in the wavefunction, while $d_{5/2}$ was the next available orbit (solid line). Therefore, the valence particle configuration of the yrast band should have been $\pi g_{7/2} \otimes \nu h_{11/2}$, as suggested by Moon *et al.* [10]. However, we assigned the proton configuration as $d_{5/2}$ based on further theoretical analysis, described below.

We performed a set of PRM calculations to explain the observed signature splitting and signature inversion. The choice of the proton valence orbital was either $d_{5/2}$ or $g_{7/2}$ or a mixture of the two, while the valence neutron occupied the $h_{11/2}$ orbital. The calculations were tried for all the positive and negative values of the deformation parameter γ ranging from 0° to 50° with the fixed values of $\varepsilon_2 \sim 0.15$ and $\varepsilon_4 \sim 0.016$. However, For the entire range of spins, below and above the signature inversion, the values of the deformation parameters (ε_2, ε_4, and γ) were kept constant. None of these calculations could reproduce the experimental observation of

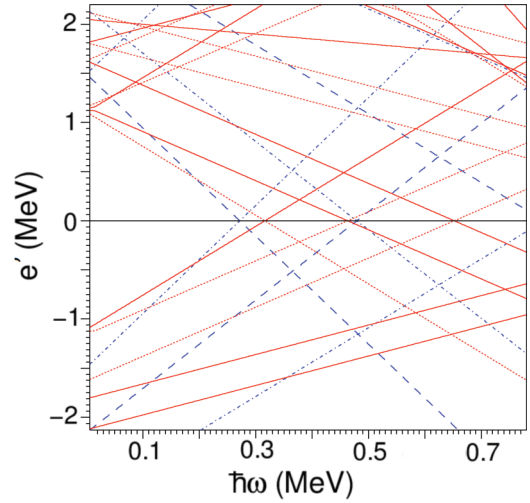

FIG. 9. (Color online) Quasiproton Routhians as a function of rotational frequency at the deformation values $\varepsilon_2 \simeq 0.15$, $\varepsilon_4 \simeq 0.016$, and $\gamma = +55^\circ$. These values correspond to the minimum in the TRS plot for the low spins (Fig. 7). Various curves are marked according to their parity and signature: solid $(+, +1/2)$, dotted $(+, -1/2)$, dash-dotted $(-, +1/2)$, and dashed $(-, -1/2)$.

signature splitting and signature inversion. The satisfactory results were obtained by using the high value of γ and changing its sign from positive to negative at the inversion spin $13\hbar$. The final values of γ was chosen to be $+45^\circ$ and -45° below and above the signature inversion, respectively, while keeping the constant values of $\varepsilon_2 \sim 0.15$ and $\varepsilon_4 \sim 0.016$. This choice was consistent with the TRS results (Figs. 7 and 8). This essentially meant that the values of the deformation parameters (ε_2, γ), used in PRM below the signature inversion, were approximately the same as those obtained through TRS at the minimum energy point in Fig. 7. Similarly, above the signature

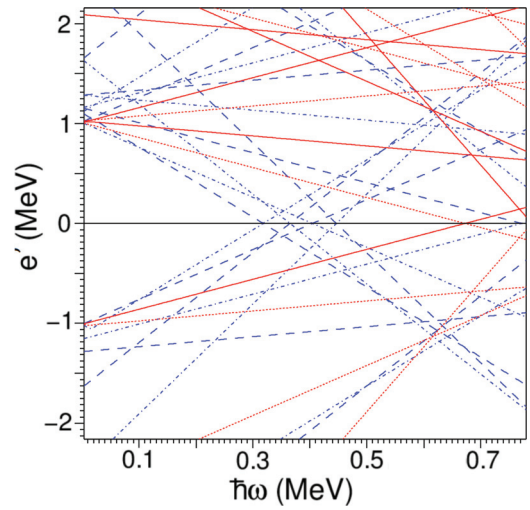

FIG. 10. (Color online) Quasineutron Routhians as a function of rotational frequency at the deformation values $\varepsilon_2 \simeq 0.15$, $\varepsilon_4 \simeq 0.016$, and $\gamma = +55^\circ$. These values correspond to the minimum in the TRS plot for the low spins (Fig. 7). Various curves are marked according to their parity and signature: solid $(+, +1/2)$, dotted $(+, -1/2)$, dash-dotted $(-, +1/2)$, and dashed $(-, -1/2)$.

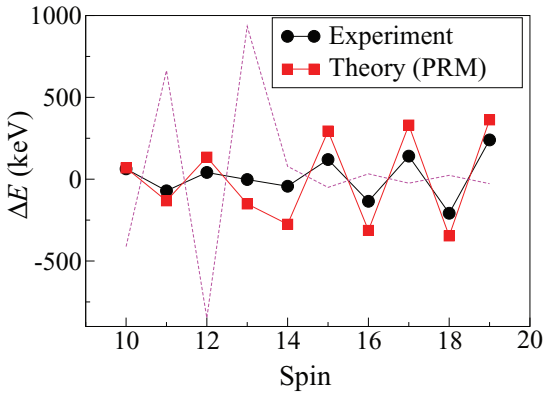

FIG. 11. (Color online) Plot of ΔE vs I for Band 3 showing the signature splitting and signature inversion. The theoretical plot (in red) is for the valence particle configuration $\pi d_{5/2} \otimes \nu h_{11/2}$. The dotted curve is the theoretical result for the valence particle configuration $\pi g_{7/2} \otimes \nu h_{11/2}$ showing a disagreement with the experiment. The details are discussed in the text.

inversion, the deformation parameters were roughly the same as those obtained through TRS at the minimum energy point in Fig. 8. At the inversion point, the rotational motion of the core nucleus was viewed as the change in the axis of rotation from the shortest axis to the intermediate axis. Although the rotation around the shortest axis cannot be realized for the hydrodynamical moment of inertia used in PRM, such a rotation is possible at the low spins, because the collective contribution to the total angular momentum is small [15]. The values of the deformation parameters (ε_2 and γ) that we inferred from the TRS calculation differed significantly from the arbitrary choice made by Zheng *et al.* [13]. The Nilsson proton configuration was a mixture of many orbitals with $d_{5/2}$ as the predominant component (Table II). Figure 11 shows a comparison between the theoretical results and the experimental results. Although the behavior of the signature splitting and inversion was reproduced, the extent of splitting was larger than the experimental observation. The dotted line shows the result of the PRM with the same deformation parameter (ε_2, ε_4, and γ) values, but with the proton occupying another Nilsson orbit which was predominantly $g_{7/2}$. It is evident from the figure that there was a complete mismatch with the experimental curve. We thus assigned this band the valence particle configuration $\pi d_{5/2} \otimes \nu h_{11/2}$. Another argument in favor of our assignment was the restoration of normal signature splitting above the signature inversion. From the point of view of the cranking picture, the even spin corresponds to the signature quantum number $\alpha = 0$. For the favored states, $\alpha = 1/2[(-1)^{j_1-1/2} + (-1)^{j_2-1/2}]$. This implies that for the particle configuration $\pi d_{5/2} \otimes \nu h_{11/2}$ ($j_1 = 5/2$, $j_2 = 11/2$), the normal signature splitting was observed above the signature inversion. Zheng *et al.* [13] have also assigned the same configuration by utilizing a different theoretical approach.

The ratio of the reduced transition probabilities $B(M1)/B(E2)$ is often used to understand the nature of a band [42]. For nuclei with a triaxial shape, K is not a good quantum number. Hence, the numerical values calculated for Band 3 in the framework of the rotational model were approximate. Nevertheless, it was possible to estimate an effective value of the g factor for the fixed quadrupole deformation, which was indicative of the particle configuration $\pi d_{5/2} \otimes \nu h_{11/2}$.

From the observed intensity of the γ transitions, the ratio $B(M1)/B(E2)$ was estimated as

$$\frac{B(M1; I \to I-1)}{B(E2; I \to I-2)} \equiv \frac{0.697}{\lambda} \frac{[E_\gamma(I \to I-2)]^5}{[E_\gamma(I \to I-1)]^3} \times \frac{1}{(1+\delta^2)} \left[\frac{\mu_N^2}{e^2 b^2}\right], \quad (5)$$

where λ is the ratio of the intensities of $E2$ and $M1$ transitions, i.e., $I_\gamma(I \to I-2)/I_\gamma(I \to I-1)$, and E_γ is the energy of the γ transition measured in MeV. The mixing ratio δ was assumed to be zero, because the calculated values of $B(M1)/B(E2)$ were not sensitive to the exact value of δ. For the rotational model [42–44], the following expressions,

$$B(M1; I \to I-1) \equiv \frac{3}{4\pi} \mu_N^2 G_{KK}^2 \langle I K 10 | I-1 K \rangle^2, \quad (6)$$

$$B(E2; I \to I-2) \equiv \frac{5}{16\pi} e^2 Q_t^2 \langle I K 20 | I-2 K \rangle^2, \quad (7)$$

were combined to yield the theoretical ratio

$$\frac{B(M1; I \to I-1)}{B(E2; I \to I-2)} \equiv \frac{8}{5} \frac{G_{KK}^2}{Q_t^2} \frac{(2I-1)}{(I-1+K)} \times \frac{(I-1)}{(I-1-K)} \left[\frac{\mu_N^2}{e^2 b^2}\right]. \quad (8)$$

The transition quadrupole moment is defined as

$$Q_t \equiv Q_{20} \frac{\cos(\gamma + 30^\circ)}{\cos 30^\circ}, \quad (9)$$

$$Q_{20} \equiv \frac{3}{\sqrt{5\pi}} Ze(r_0 A^{1/3})^2 \varepsilon_2, \quad (10)$$

where $r_0 \simeq 1.2$ fm. The parameter G_{KK} is defined as

$$G_{KK} = K(g_{\text{eff}} - g_R), \quad (11)$$

where g_{eff} is the effective g factor of the two quasiparticles and g_R ($\equiv Z/A = 0.42$) is the rotational g factor.

The important ingredient in the calculation was the value of K, which did not have a unique value. The value of K was determined by considering only the dominant component in the Nilsson wavefunction (Table II). Following the Gallagher-Moszkowski rule [45], the value of K was obtained from the parallel coupling of $K_1 = 3/2$ and $K_2 = 9/2$, i.e., $K = K_1 + K_2 = 3/2 + 9/2 = 6$. For our calculation, we considered the energy states below the signature inversion and above the bandhead spin 8^-. Three energy states 10^-, 11^-, and 12^- were utilized to determine the ratio $B(M1)/B(E2)$ from the intensities of the decaying transitions [Eq. (5)]. The values of $B(M1)/B(E2)$ were then substituted in Eq. (8) and an average value of G_{KK}^2/Q_t^2 was determined. This value was 0.23. Independently, $Q_t^2 = 0.42\, e^2 b^2$ was determined by using Eqs. (9) and (10) for the deformation parameters, $\varepsilon_2 = 0.15$ and $\gamma = +45^\circ$. The final values were $G_{KK} = 0.38$ and $g_{\text{eff}} = 0.48$.

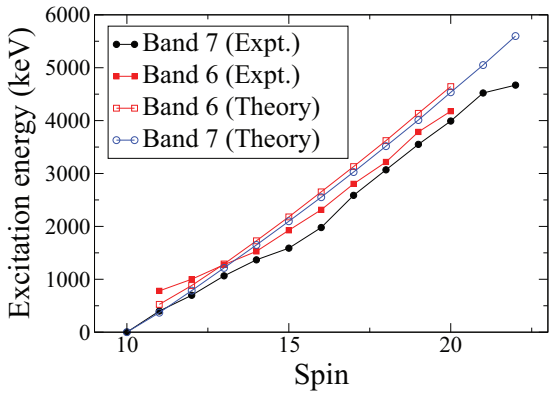

FIG. 12. (Color online) Plot of excitation energy vs. spin for Band 6 and Band 7 indicating the near degeneracy of the levels. Theoretical curves, based on the PRM, are also shown.

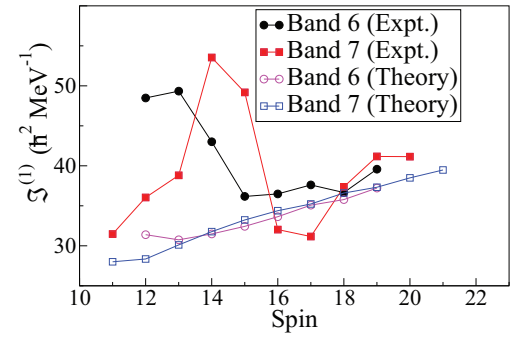

FIG. 13. (Color online) A comparison of the kinematic moment of inertia $\Im^{(1)}$ for Bands 6 and Band 7 with the theoretical results of the PRM calculations. The deformation parameter values used in the calculations were $\varepsilon_2 = 0.15$ and $\gamma = -30^\circ$.

After the above analysis, a comparison with the coupled two-quasiparticle g factor was needed. The values of the single-particle g factor were $g_\pi(g_{7/2}) = 0.677$, $g_\pi(d_{5/2}) = 1.582$ and $g_\nu(h_{11/2}) = -0.243$. These values were obtained from the reduced (0.7 times) free-particle g factors, i.e., the reduced Schmidt values. The coupled g factors for the two quasiparticles were $g(\pi d_{5/2} \otimes \nu h_{11/2}) = 0.63$ and $g(\pi g_{7/2} \otimes \nu h_{11/2}) = 0.18$. Interestingly, even with approximations used in the entire calculation, the value of $g_{\rm eff}$ was close to $g(\pi d_{5/2} \otimes \nu h_{11/2})$. This further confirmed the particle configuration to be $\pi d_{5/2} \otimes \nu h_{11/2}$.

B. Bands 6 and 7

Two positive-parity bands were observed in our experimental data. The observed bandhead spin of Band 7 was $10\hbar$, located at ~1.3 MeV above the ground state. As suggested by Zheng *et al.* [13], the valence particle configuration $\pi h_{11/2} \otimes \nu h_{11/2}$ was our best choice after inspecting the quasiparticle Routhians diagrams (Figs. 9 and 10). Band 6 and Band 7 were found to have similar characters, although Band 6 was much less in intensity than Band 7. In both the bands, the $M1$ transitions were found to be stronger than the $E2$ crossover transitions. Some weak interlinking transitions were observed that connected the low spin states of the two bands. Our theoretical interpretation of Band 6 with positive parity was completely different from the work by Zheng *et al.* [13] because of their assumption of the negative parity for this band.

To investigate if these two bands were the candidates for the chiral partners, we plotted their energy vs spin in Fig. 12. The two identical looking plots strongly suggest the possibility of them being the chiral partners. The PRM calculation was performed using the particle configuration $\pi h_{11/2} \otimes \nu h_{11/2}$. The moment of inertia parameters used were $J_0 = 22.4\ \text{MeV}^{-1}\hbar^2$ and $J_1 = 36.6\ \text{MeV}^{-3}\hbar^4$, as before. The deformation parameters (ε_2 and γ) were varied. The values finally chosen were $\varepsilon_2 = 0.15$ and $\gamma = -30^\circ$, after comparing the experimental and theoretical energies for Band 7. Also, the difference between the experimental energies of the same spin-states of Band 6 and Band 7 was compared with that of the calculated energy eigenvalues of first two eigenstates. The results of the PRM calculations are superimposed in Fig. 12 along with the experimental values. Although the theoretical values are consistently higher than the experimental values, the overall pattern of the curves is similar. When the kinematic moment of inertia, $\Im^{(1)} \equiv \frac{1}{2}(\frac{dE(I)}{dI^2})^{-1}\hbar^2\ \text{MeV}^{-1}$, was plotted as a function of spin (Fig. 13), the difference among the curves was prominent below $16\hbar$. However, above $16\hbar$ the difference became small, indicating the probable emergence of chiral behavior.

A triaxial nucleus may exhibit the chiral behavior if the three angular momenta, corresponding to each of the neutron, the proton, and the collective rotation, are oriented along the three principal axes. This was indeed observed in our PRM

TABLE II. Summary of the PRM calculations.

Band label	ε_2, ε_4	γ	Dominant particle configuration	Nilsson single-particle wavefunction
Band 1	0.15, 0	$+45^\circ$	$\pi g_{7/2} \otimes \nu h_{11/2}$	Proton: 0.58 $g_{7/2}(K=3/2)$ + 0.51 $g_{7/2}(K=1/2)$ + 0.48 $d_{5/2}(K=1/2)$ Neutron: 0.7 $h_{11/2}(K=7/2)$ + 0.50 $h_{11/2}(K=3/2)$
Band 2	0.15, 0	-45°	$\pi d_{5/2} \otimes \nu h_{11/2}$	Proton: 0.62 $d_{5/2}(K=3/2)$ + 0.41 $g_{7/2}(K=5/2)$ + 0.39 $d_{3/2}(K=1/2)$ Neutron: 0.70 $h_{11/2}(K=7/2)$ + 0.50 $h_{11/2}(K=3/2)$
Band 3	0.15, 0.016	$+45^\circ$	$\pi d_{5/2} \otimes \nu h_{11/2}$	Proton: 0.75 $d_{5/2}(K=3/2)$ + 0.40 $g_{7/2}(K=3/2)$ + 0.31 $d_{3/2}(K=1/2)$ Neutron: 0.86 $h_{11/2}(K=9/2)$ + 0.38 $h_{11/2}(K=5/2)$
Band 6,7	0.15, 0	-30°	$\pi h_{11/2} \otimes \nu h_{11/2}$	Proton: 0.76 $h_{11/2}(K=1/2)$ + 0.55 $h_{11/2}(K=3/2)$ Neutron: 0.97 $h_{11/2}(K=9/2)$

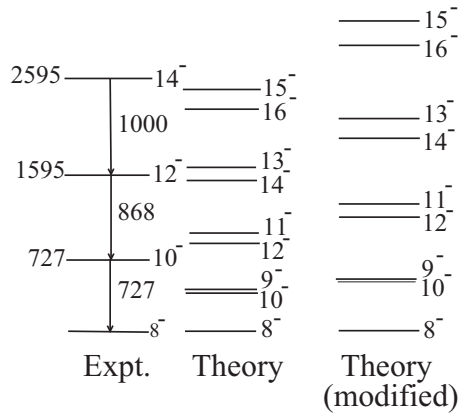

FIG. 14. A comparison of the experimental and the theoretical energy levels of Band 1. The deformation parameters used in the calculations are $\varepsilon_2 = 0.15$ and $\gamma = +45^\circ$. The levels calculated using the modified values of the Harris parameters (see text) are on the extreme right.

calculations. The average value of the square of the component of the angular momentum was found to be maximum for the proton along the x axis, the neutron along the z axis, and the collective rotation along the y axis. These values are listed in Table III for the high spin states 18^+ and 20^+, as examples. The labels x, y, and z refer to the shortest, the intermediate, and the longest principal axis, respectively. The notations p, n, and R correspond to proton, neutron, and collective rotation, respectively.

C. Bands 1 and 2

In these two bands, only the even-spin states connected with $E2$ transitions were observed. The reason might be the presence of large decoupling, which causes the odd-spin states to be pushed up sufficiently high in energy and hence they are not observed in heavy-ion fusion reactions. Such bands are called decoupled bands. We performed the PRM calculation with the valence proton predominantly occupying the $g_{7/2}$ orbit or the $d_{5/2}$ orbit and the valence neutron occupying the $h_{11/2}$ orbit. The same values of the moment of inertia parameter were used as given earlier. The value of the deformation parameter $\varepsilon_2 = 0.15$ was kept constant, but γ was varied. We obtained satisfactory results, in particular the decoupling behavior, only for $\gamma \simeq \pm 45^\circ$. The positive value of γ was used for Band 1 and the negative value for Band 2 (Figs. 14 and 15). The experimental values of the energy of the states in Band 2 were higher than those of Band 1 but the decoupling

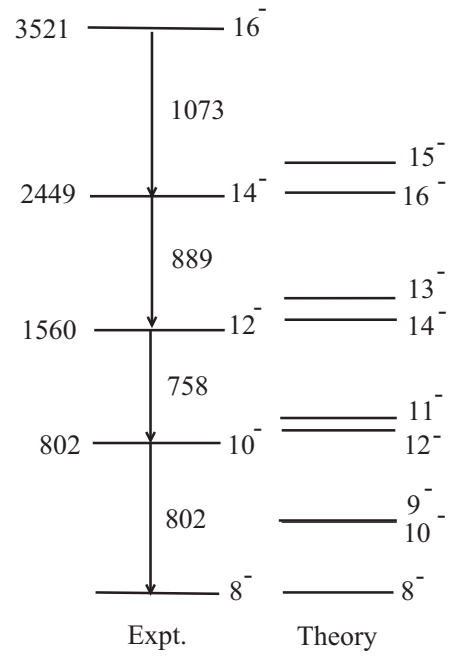

FIG. 15. A comparison of the experimental and the theoretical energy levels of Band 2. The deformation parameters used in the calculations are $\varepsilon_2 = 0.15$ and $\gamma = -45^\circ$.

behavior was the same. The Nilsson orbits are listed in Table II. Although the decoupling behavior was brought out in our calculation for both the bands, the energy of the states did not match well. In Figs. 14 and 15 the theoretical results (denoted by "Theory") are compared with the experimental results (denoted by "Expt."). Further improvement was obtained by modifying only the moment of inertia parameters, but the decoupling behavior remained the same. For instance, using the parameter values $J_0 = 25.1$ MeV$^{-1}\hbar^2$ and $J_1 = 7.3$ MeV$^{-3}\hbar^4$ and keeping all the other inputs to the PRM the same, a much better match of the theoretical results to the experimental energies was obtained. This may be seen by comparing the energy levels of Band 1, denoted by Expt., with Theory (modified) in Fig. 14. These modified parameter values were obtained by fitting the experimental energies of Band 1 itself to the Harris expansion.

D. Band 4

This band, lying high in energy, was well connected to Band 3. We inferred this band to be built on the four-

TABLE III. Expectation values of the proton, the neutron, and the rotational angular momenta in unit of $\hbar^2$, along the three principal axes, obtained through PRM calculations.

Spin	$\langle p_x^2\rangle$	$\langle p_y^2\rangle$	$\langle p_z^2\rangle$	$\langle n_x^2\rangle$	$\langle n_y^2\rangle$	$\langle n_z^2\rangle$	$\langle R_x^2\rangle$	$\langle R_y^2\rangle$	$\langle R_z^2\rangle$
18^+ (Band 7)	29	5	2	5	8	19	22	254	8
18^+ (Band 6)	29	5	2	5	8	19	24	261	7
20^+ (Band 7)	29	5	2	5	8	19	25	333	8
20^+ (Band 6)	29	5	2	5	8	19	27	337	8

quasiparticle configuration. Furthermore, the quasiparticle Routhian diagrams (Figs. 9 and 10) indicated the occurrence of the alignment of two quasineutrons at a rotational frequency lower than that for the two quasiprotons. Therefore we conjectured that two aligned neutrons were involved for this band. However, the identification of all four quasiparticles needs further investigation. There were indications for the existence of decoupling-like behavior. For instance, the energy difference between the states $21\hbar$ and $20\hbar$ was much smaller than that between the states $20\hbar$ and $19\hbar$. Further theoretical analyses are needed to completely characterize this band.

V. CONCLUSION

We have experimentally identified 27 new γ transitions in seven bands of ^{126}I and established its decay scheme up to a spin of about $23\hbar$. We have made definite parity assignments to six bands by the polarization measurement. To one of these bands (Band 6), we have assigned positive parity in contrast to the earlier report [13]. Therefore, Band 6 has become a positive-parity band instead of being a negative-parity band. The parity of one band (Band 5) is still tentative and needs to be measured experimentally.

With the confirmed assignment of spin and parity to different bands, we have investigated their properties theoretically. We have utilized two theoretical models, viz., the cranking model for TRS calculations and the PRM. The triaxial deformation has played a very important role in our theoretical analysis. The occurrence of the signature inversion in the yrast negative-parity band was linked to the change in the axis of rotation from the shortest axis to the intermediate axis of the triaxially deformed rotating nucleus. Some evidence was found for the existence of chirality in two positive-parity bands. This needs to be confirmed by measuring their electromagnetic transition probabilities. Two other negative-parity bands showed the features of decoupling behavior. Another negative-parity band, lying high in excitation energy, was probably a four-quasiparticle band, whose properties need to be investigated theoretically.

ACKNOWLEDGMENTS

The authors would like to thank V. Pasi for his help during the experiment and data analysis and V. M. Datar for critically reading the manuscript. The help provided by Deepa Thapa and A. Mahadkar in preparing the targets is gratefully acknowledged. The full cooperation of the Pelletron staff at IUAC is also thankfully acknowledged. This work was partially funded by a research grant (No. 2006/3710/BRNS/182) from the Board of Research on Nuclear Science, Department of Atomic Energy, Government of India. Bhushan Kanagalekar acknowledges the financial support from the Council of Scientific and Industrial Research, New Delhi, India.

[1] T. Koike, K. Starosta, C. J. Chiara, D. B. Fossan, and D. R. LaFosse, Phys. Rev. C **67**, 044319 (2003).
[2] V. Kumar, P. Das, S. Lakshmi, P. K. Joshi, H. C. Jain, R. P. Singh, R. Kumar, S. Muralithar, and R. K. Bhowmik, Phys. Rev. C **82**, 054302 (2010).
[3] K. Starosta, T. Koike, C. J. Chiara, D. B. Fossan, D. R. LaFosse, A. A. Hecht, C. W. Beausang, M. A. Caprio, J. R. Cooper, R. Krücken, J. R. Novak, N. V. Zamfir, K. E. Zyromski, D. J. Hartley, D. L. Balabanski, J.-Y. Zhang, S. Frauendorf, and V. I. Dimitrov, Phys. Rev. Lett. **86**, 971 (2001).
[4] F. G. Kondev *et al.*, Phys. Rev. C **59**, 3076 (1999).
[5] D. J. Hartley *et al.*, Phys. Rev. C **65**, 044329 (2002).
[6] D. J. Hartley *et al.*, Phys. Rev. C **64**, 031304 (2001).
[7] J. Burde, V. Richter, and I. Labaton, Nucl. Phys. A **402**, 205 (1983).
[8] R. N. Mathur, Indian J. Phys. **58A**, 14 (1984).
[9] J.-S. Tsai, W. V. Prestwich, and T. J. Kennett, Can. J. Phys. **64**, 1569 (1986).
[10] C. B. Moon, G. D. Dracoulis, R. A. Bark, A. P. Byrne, P. M. Davidson, A. N. Wilson, A. M. Baxter, T. Kibédi, G. J. Lane, J. C. Hazel, A. M. Bruce, N. Orce Gonzalez, F. Prades-Estevez, H. El-Masri, C. Wheldon, P. M. Walker, and R. Wood, Australian National University, Department of Nuclear Physics 2002 Annual Report, p. 17 (2003) (unpublished); ANU-P/1564 (2003) (unpublished).
[11] C. B. Moon, J. Korean Phys. Soc. **44**, 244 (2004).
[12] R.-J. Li, Y.-J. Ma, X.-G. Wu, Y.-H. Zhang, L.-H. Zhu, S.-Y. Wang, M.-F. Li, G.-D. Liang, X.-Z. Cui, X.-F. Li, G.-Y. Zhao, J.-B. Lu, Y.-Z. Liu, Z.-M. Wang, G.-S. Li, S.-X. Wen, C.-X. Yang, T. Komatsubara, and K. Furuno, High Energy Phys. Nucl. Phys. **29**(1), 1 (2005) (in Chinese).
[13] Y. Zheng, L. H. Zhu, X. G. Wu, Z. C. Gao, C. Y. He, G. S. Li, L. L. Wang, Y. S. Chen, Y. Sun, X. Hao, Y. Liu, X. Q. Li, B. Pan, Y. J. Ma, Z. Y. Li, and H. B. Ding, Phys. Rev. C **86**, 014320 (2012).
[14] B. Cederwall, F. Lidén, A. Johnson, L. Hildingsson, R. Wyss, B. Fant, S. Juutinen, P. Ahonen, S. Mitarai, J. Mukai, J. Nyberg, I. Ragnarsson, and P. B. Semmes, Nucl. Phys. A **542**, 454 (1992).
[15] A. Ikeda and S. Åberg, Nucl. Phys. A **480**, 85 (1988).
[16] Z.-C. Gao, Y. S. Chen, and Y. Sun, Phys. Lett. B **634**, 195 (2006).
[17] S. Muralithar *et al.*, Nucl. Instrum. Methods Phys. Res., Sect. A **622**, 281 (2010).
[18] B. P. Ajith Kumar, E. T. Subramaniam, K. M. Jayan, S. Mukherjee, and R. K. Bhowmik, Proceedings of the Symposium on Nuclear and Allied Instruments, India 1997, pp. 51–55.
[19] http://www.tifr.res.in/∼pell/lamps.html.
[20] M. Saha Sarkar, P. Datta, I. Ray, C. C. Dey, S. Chattopadhyay, A. Goswami, P. Banerjee, R. P. Singh, P. K. Joshi, S. D. Paul, S. Bhattacharya, R. K. Bhowmik, J. M. Chatterjee, H. C. Jain, S. Sen, and B. Dasmahapatra, Nucl. Instrum. Methods Phys. Res., Sect. A **491**, 113 (2002).
[21] D. C. Radford, Nucl. Instrum. Methods Phys. Res., Sect. A **361**, 297 (1995).
[22] D. C. Radford, Nucl. Instrum. Methods Phys. Res., Sect. A **361**, 306 (1995).
[23] K. S. Krane, R. M. Steffen, and R. M. Wheeler, Nuclear Data Tables **11**, 351 (1973).
[24] A. Krämer-Flecken, T. Morek, R. M. Lieder, W. Gast, G. Hebbinghaus, H. M. Jäger, and W. Urban, Nucl. Instrum. Methods Phys. Res., Sect. A **275**, 333 (1989).

[25] G. J. Schmid, A. O. Macchiavelli, S. J. Asztalos, R. M. Clark, M. A. Deleplanque, R. M. Diamond, P. Fallon, R. Kruecken, I. Y. Lee, R. W. MacLeod, F. S. Stephens, and K. Vetter, Nucl. Instrum. Methods Phys. Res., Sect. A **417**, 95 (1998).
[26] G. Duchêne, F. A. Beck, P. J. Twin, G. de France, D. Curien, L. Han, C. W. Beausang, M. A. Bentley, P. J. Nolan, and J. Simpson, Nucl. Instrum. Methods Phys. Res., Sect. A **432**, 90 (1999).
[27] R. Palit, H. C. Jain, P. K. Joshi, S. Nagaraj, B. V. T. Rao, S. N. Chintalapudi, and S. S. Ghugre, Pramana J. Phys. **54**, 347 (2000).
[28] K. Starosta, T. Morek, Ch. Droste, S. G. Rohoziński, J. Srebrny, A. Wierzchucka, M. Bergström, B. Herskind, E. Melby, T. Czosnyka, and P. J. Napiorkowski, Nucl. Instrum. Methods Phys. Res., Sect. A **423**, 16 (1999).
[29] V. M. Strutinsky, Nucl. Phys. A **95**, 420 (1967).
[30] G. Andersson, S. E. Larsson, G. Leander, P. Möller, S. G. Nilsson, I. Ragnarsson, S. Åberg, R. Bengtsson, J. Dudek, B. Nerlo-Pomorska, K. Pomorski, and Z. Szymański, Nucl. Phys. A **268**, 205 (1976).
[31] S. E. Larsson, Phys. Scr. **8**, 17 (1973).
[32] S. E. Larsson, G. Leander, and I. Ragnarsson, Nucl. Phys. A **307**, 189 (1978).
[33] T. Bengtsson, Nucl. Phys. A **496**, 56 (1989).
[34] T. Bengtsson, Nucl. Phys. A **512**, 124 (1990).
[35] I. Ragnarsson (private communication).
[36] M. A. J. Mariscotti, Gertrude Scharff-Goldhaber, and Brian Buck, Phys. Rev. **178**, 1864 (1969).
[37] I. Hamamoto and B. R. Mottelson, Phys. Lett. B **132**, 7 (1983).
[38] R. Bengtsson and S. Frauendorf, Nucl. Phys. A **327**, 139 (1979).
[39] R. Bengtsson, S. Frauendorf, and F.-R. May, At. Data Nucl. Data Tables **35**, 15 (1986).
[40] R. Wyss, J. Nyberg, A. Johnson, R. Bengtsson, and W. Nazarewicz, Phys. Lett. B **215**, 211 (1988).
[41] W. Nazarewicz, R. Wyss, and A. Johnson, Nucl. Phys. A **503**, 285 (1989).
[42] H. J. Chantler *et al*., Phys. Rev. C **66**, 014311 (2002).
[43] A. Bohr and B. R. Mottelson, *Nuclear Structure* (Benjamin, New York, 1975), p. 44.
[44] W. Nazarewicz and I. Ragnarsson, in *Handbook of Nuclear Properties*, edited by D. Poenaru and W. Greiner (Clarendon, Oxford, 1996), p. 80.
[45] C. J. Gallagher, Jr. and S. A. Moszkowski, Phys. Rev. **111**, 1282 (1958).